PAPER

Check for updates

Elucidation of the reaction mechanism on dry reforming of methane in an electric field by *in situ* DRIFTs†

Naoya Nakano,[a] Maki Torimoto,[a] Hiroshi Sampei, [iD][a] Reiji Yamashita,[a]
Ryota Yamano,[a] Koki Saegusa,[a] Ayaka Motomura,[a] Kaho Nagakawa,[a]
Hideaki Tsuneki,[a] Shuhei Ogo [iD][bc] and Yasushi Sekine [iD]*[a]

With increasing expectations for carbon neutrality, dry reforming is anticipated for direct conversion of methane and carbon dioxide: the main components of biogas. We have found that dry reforming of methane in an electric field using a Pt/CeO_2 catalyst proceeds with sufficient rapidity even at a low temperature of about 473 K. The effect of the electric field (EF) on dry reforming was investigated using kinetic analysis, *in situ* DRIFTs, XPS, and DFT calculation. *In situ* DRIFTs and XPS measurements indicated that the amount of carbonate, which is an adsorbed species of CO_2, increased with the application of EF. XPS measurements also confirmed the reduction of CeO_2 by the reaction of surface oxygen and CH_4. The reaction between CH_4 molecules and surface oxygen was promoted at the interface between Pt and CeO_2.

1. Introduction

As expectations for the achievement of carbon neutrality continue to rise worldwide, the effective use of biomass resources is attracting attention as one means of achieving that goal. Biogas obtained from anaerobic fermentation is composed mainly of methane and carbon dioxide, both of which are known to be greenhouse gases. A promising technology is one that could directly convert methane and carbon dioxide into high value-added substances such as synthesis gas by dry reforming (DRM: eqn (1)).[1,2] However, because of thermodynamic and kinetic constraints, the conventional catalytic process for dry reforming requires temperatures higher than 1000 K. Moreover, the reaction is known to be prone to carbon deposition.

$$DRM: CH_4 + CO_2 \rightarrow 2CO + 2H_2, \Delta H^0_{298} = 247 \text{ kJ mol}^{-1} \quad (1)$$
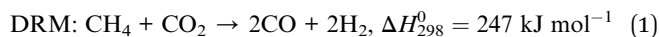
The reaction mechanism of CO_2 in these reactions has been well-studied through *in situ* DRIFTs measurements. CO_2 dissociates on the active metal *via* carbonyl species[3–6] and supports oxides using oxygen vacancies *via* intermediates such as

carbonate and formate.[7–10] Chen *et al.*[11] reported that CO was formed *via* carbonate, which is adsorbed species of CO_2 using CeO_2 lattice oxygen defects, in DRM using Pt–Ni supported CeO_2. Bobadilla *et al.*[12] revealed that the reaction proceeds *via* formate species as the key intermediate in RWGS (reverse water gas shift) of Pt-loaded CeO_2.

In addition, various unconventional studies have been conducted in recent years to promote the conversion of CO_2 by application of external stimuli such as electricity, magnetic fields, and light.[13–17] Wang *et al.* reported that Xe lamp irradiation to Cu-loaded CeO_2 increases the amount of lattice defects of CeO_2 and shows high CO_2 reduction performance.[18] Zhu *et al.*[19] reported that plasma application accelerates the formation and decomposition of the intermediate formate in DRM using Au-loaded CeO_2. Consequently, a process that accelerates the reaction by providing an external stimulus is becoming a more attractive CO_2 conversion technology.[20,21]

Under these circumstances, our group has proposed a catalytic reaction in an electric field (EF) in which direct current is applied by inserting electrodes at the top and bottom edges of the catalyst layer to promote the reaction.[22–25] We earlier reported various effects of enhanced activity and lowered apparent activation energy at low temperatures in DRM,[26] RWGS,[27] and CO_2 methanation.[28]

However, details of the reactivity of CO_2 and its adsorption ability in the EF have not been clarified. Therefore, *in situ* DRIFTs measurements were taken for this study to confirm EF effects on the CO_2 conversion reaction by examining changes of intermediates when the EF is applied during a DRM reaction.

[a]Department of Applied Chemistry, Waseda University, 3-4-1, Okubo, Shinjuku, Tokyo, 169-8555, Japan. E-mail: ysekine@waseda.jp

[b]Department of Marine Resources Science, Faculty of Agriculture and Marine Science, Kochi University, Nankoku, 783-8502, Japan

[c]Center for Advanced Marine Core Research, Kochi University, Nankoku, 783-8502, Japan

† Electronic supplementary information (ESI) available. See DOI: 10.1039/d2ra00402j

© 2022 The Author(s). Published by the Royal Society of Chemistry

2. Experimental

2.1 Catalyst preparation

The catalyst of 1 wt% Pt-supported ceria (1wt%Pt/CeO$_2$) was prepared using an impregnation method. We used ceria (CeO$_2$; JRC-CEO-1) supplied by the Catalysis Society of Japan as a support. Pt was loaded on the support using the following procedure. First, Pt(NH$_2$)$_4$(NO$_3$) (Sigma-Aldrich Corp.) was dissolved in distilled water. The powder of CeO$_2$ support was added to the solution and was stirred for 2 h. Subsequently, the solution was dried at 393 K for 24 h. The obtained powder was calcined at 773 K for 3 h. The obtained sample was pressed and sieved using 355–500 μm mesh. Subsequently it was reduced with 20% H$_2$ diluted with Ar at a 100 SCCM flow rate at 723 K for 30 min.

2.2 In situ diffuse reflectance infrared Fourier transform spectroscopy (DRIFTs)

In situ DRIFTs measurements were taken with an FT-IR spectrophotometer (FT/IR-6200; Jasco Corp.) equipped with a ZnSe window and MCT-M detector cooled with liquid nitrogen. Spectra were recorded with 4 cm^{-1} resolution and 50–200 times scans. The DRIFT cell was made of PTFE, which is an insulator for inserting two electrodes as described in an earlier report.[29] After a pelletized catalyst of 50 mg (without EF) or 110 mg (with EF) was set in the DRIFT cell, the EF was applied with 3 mA of direct current. A schematic image of the DRIFT cell was described in an earlier report.[29] The background spectrum was recorded under Ar flow at 90 SCCM at 473 K without EF. During the experiment, CH$_4$ and CO$_2$ were supplied respectively at 10 SCCM. They were diluted with Ar at 90 SCCM at 473 K.

2.3 Activity test

Catalytic activity tests were conducted with a fixed bed flow type reactor as presented in Fig. S1.† A 6.0 mm-diameter quartz tube was used, with 300 mg of the catalyst charged in it. A thermocouple was inserted into the catalyst bed at the bottom. The reaction temperature was fixed at 473 K. The temperature was controlled with the thermocouple of the catalyst bed, which includes the Joule heat with EF. For that reason, electrical heating of the catalyst bed is negligible in this case. The feed gas (Ar : CH$_4$: CO$_2$ = 2 : 1 : 1) was supplied with the total flow rate of 80 SCCM. A direct current voltage power supply was used to apply the EF. The current and applied voltage were monitored using a digital phosphor oscilloscope (TDS2100; Tektronics Corp.). After passing a cold trap, the reacted gas was analyzed using GC-FID, TCD (GC-2014; Shimadzu Corp.) with a Porapak Q column and a methanizer. The conversion, yield, and input power were calculated by some equations (see ESI†).

2.4 Characterization

Powder X-ray diffractometry (XRD, RINT-Ultima III; Rigaku Corp.) was used to characterize the crystalline structure of catalysts before and after the activity test. The anode voltage and current were 40 kV, 40 mA, respectively, with Cu-Kα radiation.

Fig. S2† shows XRD patterns of catalysts before and after the activity test. The diffraction peaks at 28.6, 33.0, 47.4, 56.4, 69.3, and 76.7° were assigned respectively to the CeO$_2$ crystal facets of (111), (200), (220), (311), (222), and (400). No significant change in the crystalline structure occurred during the reaction.

The nitrogen physical ad-/desorption isotherm of catalysts was measured using a surface area analyser (Gemini VII; Micromeritics Instrument Corp.) at 77 K. The specific surface area was obtained using the BET method. The specific surface area of the catalyst before the activity test was 158 m^2 g^{-1}.

The Pt particle size was measured using a field-emission electron microscope (FE-TEM, JEM-2100F; Jasco Corp.) with 200 kV accelerating voltage and 0.1 nm resolution. Fig. S3† shows HAADF-STEM images and EDX mappings of 1wt%Pt/CeO$_2$. The image of elemental mapping shows that Pt was highly dispersed on CeO$_2$ and that the particle size could not be estimated. The Pt loading amount on the catalyst was confirmed by ICP-OES. The X-ray photoelectron spectroscopy (XPS) measurements were taken (PHI 5000 Versa Probe II; ULVAC-PHI Corp.) with a monochromatic Al-Kα X-ray source. Before the measurement, samples were pretreated with H$_2$ (H$_2$: Ar = 1 : 4; 100 SCCM total flow rate) and O$_2$ (O$_2$: Ar = 1 : 4; 100 SCCM total flow rate) at 693 K for 30 min. Subsequently they were exposed to CH$_4$, CO$_2$, and Ar flow, respectively, for 20 min. In each flow, the EF was applied for 10 min at 3 mA. The samples were transported to the instrument using a transfer vessel while avoiding exposure to air. The obtained binding energies were calibrated using C 1s assigned to C–H or C–C (284.8 eV). The peak fittings were conducted using the Shirley method.[30] The Ce^{3+} fraction was calculated using the equation shown in ESI.†

2.5 DFT calculation

All Density Functional Theory (DFT) calculations were performed using the Vienna Ab initio Simulation Package (VASP) 5.4.4 with the PAW (Projector Augmented Wave) potentials.[31–33] The Perdew–Burke–Ernzerhof (PBE) of the generalized gradient approximation (GGA) was used as the functional, and the van der Waals force was corrected by DFT-D3.[34,35] The plane wave cutoff was set to 400 eV, and the on-site Coulomb interaction of Ce 4f orbitals was taken into account using the DFT+U method with U = 5.0 eV.[36–41] As reciprocal space sampling, $(5 \times 5 \times 5)$ and $(1 \times 1 \times 1)$ k-points were sampled using Gaussian smearing for CeO$_2$ bulk and slab, respectively, and 0.08 Å^{-1} k-points were sampled using the first order Methfessel–Paxton method for Pt bulk.[42] All sampling points were decided with Monkhorst–Pack method.[43]

The calculated lattice constant of CeO$_2$ bulk was 5.437 Å with an error of 0.4% from the experimental value.[44] The CeO$_2$(111) slab was represented by the three repeated layers of (3×6) supercells with 20 Å vacuum layers. The lowest layer was fixed during the structural optimization. The calculated lattice constant of Pt bulk was 3.909 Å with an error of 0.4% from the experimental value.[45] A Pt rod were prepared from the (111) and (100) planes of the Pt bulk as the side and top, respectively, and placed on a CeO$_2$ slab to express Pt/CeO$_2$ surface. The O$_2$

molecules in the gas phase were placed in a $10 \times 10 \times 10$ Å box and calculated at Γ point. All calculation models were depicted using VESTA.[46] (Fig. S13 and S14†) In addition, the oxygen vacancy formation energies were calculated according to the following equation.

$$E_{\text{Vox}} = E(\text{Pt/CeO}_2 \text{ without O}) + (\tfrac{1}{2}E(\text{O}_2) - E(\text{Pt/CeO}_2)) \quad (2)$$

Here, E_{Vox}, $E(\text{O}_2)$, and $E(\text{Pt/CeO}_2)$, $E(\text{Pt/CeO}_2 \text{ without O})$ are the energy of the formation energy of the oxygen defect, the oxygen molecule, the Pt/CeO$_2$ model, the Pt/CeO$_2$ model after the oxygen defect formation, respectively.

3. Results and discussion

3.1 Catalytic activity

First, activity tests were performed to evaluate the activity with EF at low temperatures. Yabe *et al.*[26] reported DRM activity with EF: the reaction proceeds at a temperature as low as 473 K for Ni-supported La-doped ZrO$_2$ with EF. As the catalyst, Pt/CeO$_2$ was selected because CeO$_2$ has been studied for other reactions with EF, such as methane steam reforming[29] and dehydrogenation of methylcyclohexane.[47] Then, Pt/CeO$_2$ catalysts with various supported amounts of Pt were investigated (Fig. S4†), and 1wt%Pt/CeO$_2$ showed highest activity and was selected for suitable catalyst. Table 1 presents the catalytic activity of 1wt% Pt/CeO$_2$ at 473 K. The activities at different temperatures are presented in Table S1.† Fig. S5† shows the relation between reaction temperature and conversion in DRM (left), the Arrhenius plot (middle), and H$_2$/CO ratio (right). The conversion of CH$_4$ and CO$_2$ at 473 K was more than 15% (it is conducted in a kinetic region), whereas the reaction did not proceed without EF at this temperature. The cause of catalyst deactivation, the amount of carbon deposition, was negligible because the carbon balance was almost 100%. No carbon formation on the catalyst was apparent after the reaction. The apparent activation energy calculated from the Arrhenius plot (Fig. S5†) without EF was 104 kJ mol^{-1}, but it was markedly lower with EF: only 4.82 kJ mol^{-1}. As reported from an earlier study, the H$_2$/CO ratio with EF was high in the low-temperature range.[26] In addition, the power efficiency, the value obtained by dividing the gained

enthalpy during the reaction by the applied power, was calculated as around 20%. As described above, the 1wt%Pt/CeO$_2$ showed high activity for DRM at 473 K in the electric field. Therefore, we investigated the reaction pathway related to this process using various methods including DRIFTs.

3.2 Effects of EF on CO$_2$ adsorption

To elucidate reasons why DRM proceeds effectively even at such low temperatures, *in situ* DRIFTs measurements were performed to observe the changes in CO$_2$ adsorption state before and after applying the EF. The adsorption of CO$_2$ on CeO$_2$-based catalysts has been well-studied. Many reports have assigned the peaks of carbonaceous species. The assignment of carbonaceous species used for this study and their values in the literature are shown in ESI.†[5,11,48-73] We assigned peaks in the range of 1800–2100 cm^{-1} to carbonyl species adsorbed onto Pt, but they are not shown in the table. In this measurement, we applied the EF to the catalyst in the CO$_2$ flow and compared the spectra before and after the application of EF. Fig. 1 shows (a) DRIFT spectra before and after the application of EF and (b) the difference spectrum obtained by subtracting the spectrum without EF from that with EF. As shown in Fig. 1(b), the peak area at around 1160 cm^{-1} was increased by the application of EF. The peaks at 1160, 1131, 1074, and 1031 cm^{-1} are assigned
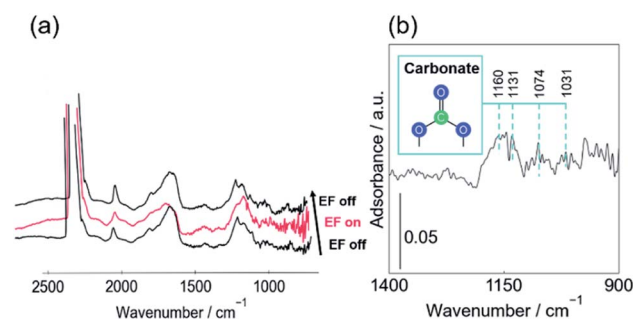

Fig. 1 (a) *In situ* DRIFT spectra with, without EF under CO$_2$ flow over 1wt%Pt/CeO$_2$, (b) difference spectra in 900–1400 cm^{-1} region (with EF − without EF); CO$_2$: Ar = 1 : 8; 90 SCCM total flow rate; 3.0 mA input current; at 473 K.

Table 1 Catalytic activities over 1wt%Pt/CeO$_2$ catalyst with/without the electric field (EF)

	Temp./K	CH$_4$ conv./%	CO$_2$ conv./%	H$_2$/CO/—	Power/W	Energy efficiency/—
With EF	453	15.1	16.4	0.763	2.81	0.186
	473	15.0	16.5	0.754	2.91	0.179
	523	15.9	17.9	0.728	2.74	0.203
	573	16.4	19.2	0.696	2.61	0.223
	623	17.4	20.9	0.667	2.54	0.244
	672	19.1	24.0	0.625	2.63	0.262
	723	27.5	34.6	0.623	2.87	0.347
Without EF	472	0	0	—	—	—
	523	0.00	0.01	0.00	—	—
	573	0.03	0.07	0.00	—	—
	623	0.15	0.42	0.00	—	—
	673	0.66	1.60	0.135	—	—
	723	2.21	4.75	0.237	—	—

respectively as monodentate, bridged, polydentate, and bidentate carbonate peaks (see ESI†). The increase of the peak area at around 1160 cm^{-1} signifies that the number of carbonate species adsorbed onto CeO_2 increased because of application of the EF.

In general, CO_2 adsorbs on metal oxides and forms adsorbed species such as carbonate and bicarbonate.[71,74] DFT calculations and various experimentally obtained results revealed that lattice oxygen defects enhance the adsorption of gas-phase CO_2.[75–77] Lattice oxygen in the catalyst support dissociates CH_4 in the DRM reaction, leading to the formation of oxygen vacancies.[75,78,79]

Consequently, the reaction of CH_4 with lattice oxygen is expected to be an important factor supporting oxygen vacancy formation. Therefore, to investigate the effects of CH_4 on the formation of lattice oxygen defects with or without EF, we took XPS measurements and evaluated the reducibility of CeO_2. We then compared the fractions of Ce^{3+} and Ce^{4+} of 1wt%Pt/CeO_2 after exposing catalysts to CH_4, CO_2, and Ar flow, respectively with and without EF at 473 K. Table 2 shows the calculated Ce^{3+} fraction of 1wt%Pt/CeO_2 spent in each condition. Fig. S7† presents the obtained XPS spectra. In the Ce 3d spectrum, three doublet peaks at (u‴: 916.6, v‴: 898.2), (u″: 907.5, v″: 888.8), and (u: 900.7, v: 882.3) eV are assigned to Ce^{4+}; two doublet peaks at (u′: 903.8, v′: 885.2), (u$_0$: 899.3, v$_0$: 880.7) eV are assigned to Ce^{3+}.[80] Table 2 shows that the fraction of Ce^{3+}, after being kept in the CH_4 flow with EF, was larger than that without EF. The increase in the Ce^{3+} fraction in the CH_4 flow suggests that the oxygen species were removed easily by reaction with CH_4 in the EF, resulting in the formation of more lattice oxygen defects. Fig. S8† depicts changes in DRIFT spectra before and after application of the EF under the CH_4 flow. Fig. S8† (b) shows that the peak area of carbonate species increased. The increase of the carbonate species signifies that CH_4 consumed lattice oxygen, which is the only oxygen source, resulting in the formation of lattice oxygen defects.

The increase of Ce^{3+} fraction by application of the EF in Ar flow was 0.5%, which is much less than that in the CH_4 flow. Therefore, the oxygen species are not released simply by application of the EF, but are released by the reaction with CH_4 in the EF. Therefore, the oxygen of CeO_2 is regarded as activated by the EF. Thus the reaction of lattice oxygen with CH_4 is promoted, thereby forming the oxygen defect.

The fraction of Ce^{3+} increased from 17.5% to 18.3% after applying the EF in the CO_2 flow, indicating an increase of carbonate species by CO_2 adsorption. According to Yi et al.,[81] Ce^{4+} decreases along with the carbonate species formation because the carbonate species are formed by oxidization of the adsorbed CO_2 by the surface oxygen of the CeO_2 support. Therefore, the reduction of Ce in the EF in the CO_2 flow also supports enhancement of the CO_2 adsorption.

The enhanced reactivity of oxygen in the EF was confirmed using oxygen isotope exchange test. Fig. S9† portrays results of the oxygen isotope exchange test. For this measurement, the EF was applied to the catalyst in the $^{18}O_2$ flow after the surface oxygen species in CZO were filled with ^{16}O. Then a mass spectrometer was used to analyze the produced gas. As shown in Fig. S9,† after the application of EF, the amount of $^{18}O_2$ decreased immediately. Simultaneously, $^{16}O^{18}O$ appeared. However, the appearance of $^{16}O_2$ was slight. These results indicate that lattice oxygen is not removed merely by applying EF. Rather, it is removed by reaction with the gas species. This result also supports the increased reactivity of the oxygen in the EF.

3.3 Reactivity of carbonate species

Next, an alternating feed test between CO_2 and CH_4 was conducted to elucidate the behaviour of CO_2 and CH_4 in the DRM reaction with and without EF. In the alternating feed test, CO_2 and CH_4 were switched; GC was used to analyze the produced gas. Fig. 2 shows the calculated formation rate of CO after switching the gas with EF. Actually, CO was not observed without EF, although it was formed with EF. The CO formed after either the CO_2 or CH_4 supply. This CO formation signifies that oxidation of CH_4 and reduction of CO_2 occur on Pt/CeO_2 with EF. In both gas feeds, the amount of the produced CO decreased with the time course. The oxidation and reduction performance of the catalyst decreased with time because of the continuous supply or consumption of oxygen. From earlier results and research, we assumed the role of lattice oxygen in this test. In the CH_4 flow, lattice oxygen was removed by CH_4. Then depletion of the activated oxygen caused the decrease of the produced CO amount. However, CO_2 filled the lattice oxygen defect in the CO_2 flow. The amount of produced CO decreased along with the decrease of the lattice oxygen defects.
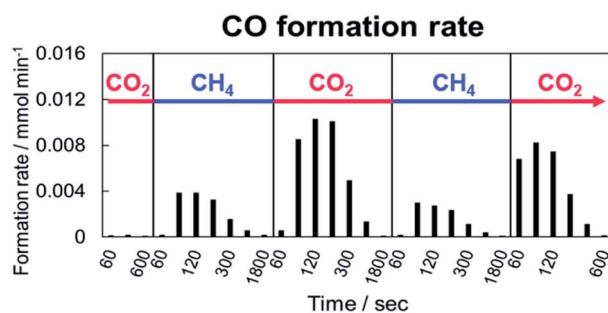
Table 2 Relative ratio of surface contents of Ce^{3+}

Condition	Surface content of Ce^{3+}/%
CH_4 flow without EF	16.8
CH_4 flow with EF	19.4
Ar flow without EF	16.2
Ar flow with EF	16.7
CO_2 flow without EF	17.5
CO_2 flow with EF	18.3

Fig. 2 CO formation rate after switching between CO_2 and CH_4 over 1wt%Pt/CeO_2 catalyst with EF; 80 SCCM total flow rate (CH_4 : Ar = 1 : 3 under CH_4 flow, CO_2 : Ar = 1 : 3 under CO_2 flow) at 473 K.

In situ DRIFTs measurements were conducted in the CO_2, CH_4 alternating feed test to observe the reactivity of the carbonate species. Fig. 3 portrays the change in spectra in the test between CH_4 and CO_2 (a) with EF, (b) without EF, and the difference in the spectrum before and after CH_4 supply (c) with EF, (d) without EF. The peaks assigned to carbonate species decreased by stopping the CO_2 supply, irrespective of the presence of EF. A similar decrease in the carbonate peak was observed when the supply gas was switched from CO_2 to Ar without EF (Fig. S10 and S11†). Without EF, CO was not formed when the CO_2 gas feed was switched to CH_4 or Ar flow, suggesting that carbonate species desorbed as CO_2. However, when the EF was applied, CO was formed, suggesting that some of the carbonate species reduced and dissociated as CO.

3.4 Oxygen release ability of CeO₂

DFT calculations were performed to investigate the tendency of oxygen defect formation on Pt-loaded CeO_2. Fig. S15† shows the calculated oxygen defect locations, and Table S3† shows the oxygen defect formation energy at each location. The formation energy of the oxygen defects became higher as the distance from Pt increased. The results show that the oxygen defects are more easily generated at the interface of Pt and CeO_2 than other locations. This result supports the reaction of CO_2 at the interface of Pt and CeO_2 because the oxygen defects are more easily generated near the interface, and the generated oxygen defects facilitate the adsorption of CO_2 near the interface.[75] Note that the sign of the value does not mean whether it is spontaneous or not, because the energy of half of the oxygen

molecule is used as the energy of the oxygen atom and the term of pressure, and the temperature is not taken into account in the calculation of the oxygen defect formation energy.

3.5 Discussion

From these results, we consider the effect of EF on DRM and the reaction mechanism.

3.5.1 Effect of EF. *In situ* DRIFTs measurements revealed the effect of the EF on CO_2 adsorption. As shown in Fig. 1, the peak area of carbonate species increased by application of the EF, indicating that application of the EF enhanced the CO_2 adsorption. The XPS measurement results also support the enhancement of CO_2 adsorption on CeO_2 (Table 2).

It is reported that the enhancement in CO_2 adsorption is related to the oxygen activity of the oxide support. Chen et al.[82] investigated the adsorption and oxidation, redox behaviour of CO and CO_2 on CeO_2 using DFT calculations. They reported that highly reactive surface oxygen, which Ce weakly bonds, lowers CO_2 adsorption and carbonate species formation barriers. In addition, results of several studies suggest that EF promoted the activation of the oxygen in the oxide support.[83–85] High catalytic activity due to the activated oxygen on supports by applying EF was reported in the OCM reaction using CeO_2,[85] and in the TWC catalytic reaction of exhaust gases using cerium zirconium oxides ($Ce_{0.7}Zr_{0.3}O_2$) as support.[84] Therefore, we considered that lattice oxygen was activated by the EF, and promoted CO_2 adsorption.

The XPS measurements taken for this study revealed that CH_4 molecules react with surface oxygen, consume them, and thereby reduce CeO_2 more with EF than without EF (Table 2). This improved reactivity of CH_4 with surface oxygen might be attributed to the enhanced reactivity of the oxygen by the EF.

Next, the CO_2, CH_4 alternating test shows the CO_2 dissociation ability of CeO_2. When the gas was switched from CO_2 to Ar without EF, the carbonate species desorbed as CO_2 (Fig. S9 and S10†). When the gas was switched to CH_4 without EF, the carbonate species also desorbed as CO_2 and CO did not form. However, CO was formed when the supply gas was switched to CH_4 with EF, indicating that a part of the carbonate species reacted and desorbed as CO (Fig. 2 and 3). These results indicate that the EF promotes dissociation of CO_2 adsorbed on CeO_2.

3.5.2 Active site. DFT calculations showed that oxygen defect is likely to form on CeO_2 at the interface of Pt and CeO_2. Previous research suggest that oxygen defect promotes CO_2 adsorption.[75] Thus, CO_2 adsorption tends to occur on CeO_2 at the interface of Pt and CeO_2.

On the other hand, CH_4 dissociates on Pt at the interface of metal (Pt) and support (CeO_2) with EF[75] and without EF.[86,87] CH_4 and CO_2 with high reactivity at the interface of Pt and CeO_2 suggests that active site of this reaction is the interface of Pt and CeO_2.

3.5.3 Reaction mechanism. From these results, we considered the possible DRM mechanism.

First, with the EF, the reaction of CO_2 is considered to proceed by the Mars–van Krevelen (MvK) mechanism using the lattice oxygen of the support. Yabe et al.[75] have shown that the dissociation of CO_2 proceeds *via* the lattice oxygen in the EF by
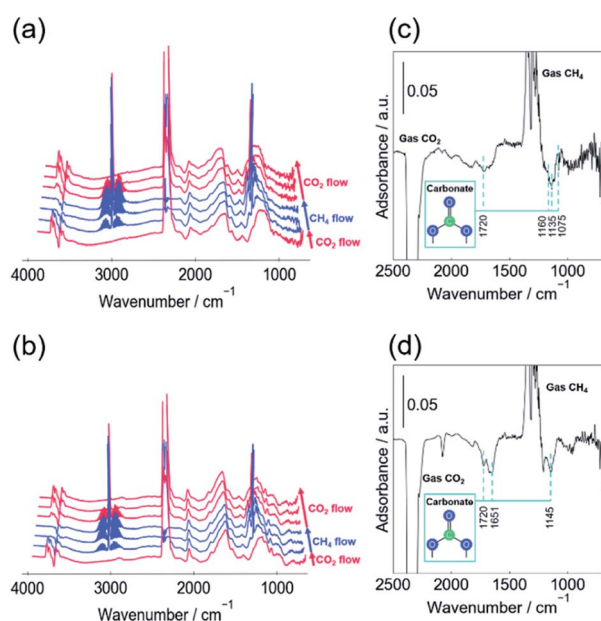

Fig. 3 *In situ* DRIFT spectra over 1wt%Pt/CeO₂ catalyst after switching between CO_2 and CH_4 feeds at 473 K. 120, 600, 1200 seconds after switching to CH_4, 120, 600, 1200 seconds after switching to CO_2, (a) with (b) without EF; difference spectrum in 700–2500 cm⁻¹ (CH_4 at steady state − CO_2 at steady state) (c) with (d) without EF; 90 SCCM total flow rate (CH_4 : Ar = 1 : 8 under CH_4 flow, CO_2 : Ar = 1 : 8 under CO_2 flow at 473 K); 3.0 mA input current.
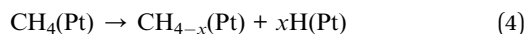
^{18}O isotope test. This indicates that the dissociation of CO_2 by the MvK mechanism proceeds at low temperatures with EF.
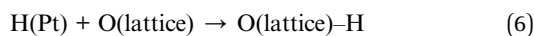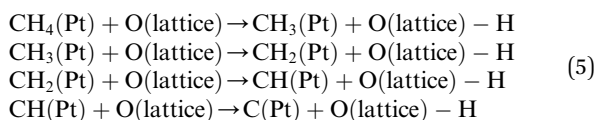
Contrarily, CH_4 dissociation proceeds on Pt. Previously, many reports have suggested the rate determining step (RDS) of the reaction of CH_4. Otsuka *et al.*[88] showed that CH_4 dissociation and recombination proceed much faster than the oxidation of CH_4 on CeO_2 and Pt/CeO_2 by the CH_4, CD_4 exchange test. Wei and Iglesia[89] also suggested C–H bond activation on Pt is reversible, using the CH_4, CD_4 exchange test in DRM reaction. Thus, the oxidation of H species formed after CH_4 dissociation is necessary for the reaction to proceed. Das *et al.*[86] have also reported that reaction of CH_4 and lattice oxygen is the RDS in the DRM reaction. Therefore, we considered that the RDS in this reaction is oxidation of the H species. The EF promotes the reaction to activate lattice oxygen.

From these results, we considered the possible DRM mechanism as follows.
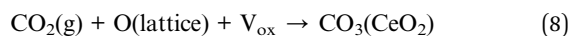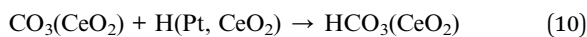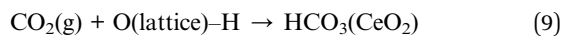
(1) Methane dissociation on Pt[90]

$$CH_4(g) \rightarrow CH_4(Pt) \tag{3}$$

$$CH_4(Pt) \rightarrow CH_{4-x}(Pt) + xH(Pt) \tag{4}$$

(2) Diffusion of H species[86,90]

$$CH_4(Pt) + O(lattice) \rightarrow CH_3(Pt) + O(lattice) - H$$
$$CH_3(Pt) + O(lattice) \rightarrow CH_2(Pt) + O(lattice) - H$$
$$CH_2(Pt) + O(lattice) \rightarrow CH(Pt) + O(lattice) - H \tag{5}$$
$$CH(Pt) + O(lattice) \rightarrow C(Pt) + O(lattice) - H$$

$$H(Pt) + O(lattice) \rightarrow O(lattice)\text{–H} \tag{6}$$

(3) Methane desorption as CO[86]

$$C(Pt) + O(lattice) \rightarrow CO + V_{ox} \tag{7}$$

(4) CO_2 adsorption

$$CO_2(g) + O(lattice) + V_{ox} \rightarrow CO_3(CeO_2) \tag{8}$$

(5) Hydrogenation of CO_2 species

$$CO_2(g) + O(lattice)\text{–H} \rightarrow HCO_3(CeO_2) \tag{9}$$

$$CO_3(CeO_2) + H(Pt, CeO_2) \rightarrow HCO_3(CeO_2) \tag{10}$$

(6) Desorption of carbonaceous species

$$HCO_3(CeO_2) + H(Pt, CeO_2) \rightarrow CO(g) + H_2O(g) + O(lattice) + V_{ox} \tag{11}$$

$$HCO_3(CeO_2) \rightarrow CO(CeO_2) + O(lattice)\text{–H} + O(lattice) \tag{12}$$
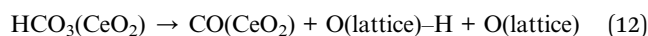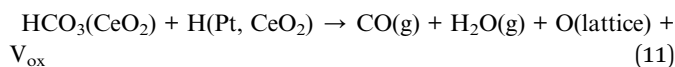
(7) Refilling of oxygen vacancy

$$V_{ox} + H_2O \rightarrow O(lattice) + 2H(CeO_2) \tag{13}$$

(8) Formation of H_2

$$2H(CeO_2) \rightarrow H_2(g) \tag{14}$$

$$2H(Pt) \rightarrow H_2(g) \tag{15}$$
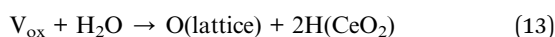
Here, V_{ox} and O(lattice) denote oxygen vacancy and lattice oxygen, respectively.

First, the EF effect is to enhance the oxygen activity of oxide support because the adsorption of CO_2 was promoted significantly by EF application (eqn (8)). The activated surface oxygen reacts easily with C and H species dissociated from CH_4 and forms oxygen defects (eqn (5)–(7)).

The activated oxygen and the oxygen defects of oxide support both contribute to enhancement of the CO_2 adsorption. Finally, the adsorbed CO_2 forms carbonate species, reacts, and desorbs as CO. The remaining oxygen species again work as the oxidant of CH_4. Consequently, the DRM reaction in the EF proceeds *via* a redox cycle of CeO_2 support.

4. Conclusion

The effect of the electric field (EF) on DRM reaction was investigated using 1wt%Pt/CeO_2 by activity tests, *in situ* DRIFTS, XPS, and DFT calculation. 1wt%Pt/CeO_2 showed high activity for DRM with EF, even at 473 K, at which thermal catalysis proceeds only slightly. *In situ* DRIFTs measurements in CO_2 flow revealed that the adsorbed species of CO_2 increases when the EF is applied. This increase signifies that the adsorption of CO_2 is promoted by the EF. XPS measurements of the catalysts after the treatment in CO_2 atmosphere with EF suggest the enhancement of CO_2 adsorption on CeO_2. In addition, XPS measurements of catalysts after exposure to CH_4 flow with EF confirmed that the Ce^{3+} fraction of CeO_2 increased, indicating that CeO_2 support was reduced after the reaction of surface oxygens and CH_4 molecules in EF, even at 473 K. These results suggest that the oxygen in the oxide support was activated in the EF. Furthermore, the reaction of CH_4 and the surface oxygen was promoted, thereby forming lattice oxygen defects and CO. The activated oxygen in the EF and the resulting lattice oxygen defects by the reaction with CH_4 molecules both promote CO_2 adsorption. The reaction is considered to proceed at the interface of Pt and CeO_2. DFT calculations also support the reaction mechanism of DRM at the interface of Pt and CeO_2.

In summary, the reaction mechanism of DRM in the EF was inferred as presented below. The EF can improve the oxygen activity and can therefore promote the reaction of CH_4 molecules and surface oxygens at the Pt–CeO_2 interface, forming the oxygen defects. Both the activated oxygen and the oxygen defects of oxide support enhance the adsorption of CO_2, forming more carbonate species on CeO_2 in the EF. Finally, CO_2 molecules dissociate to form CO *via* the carbonate species.

Conflicts of interest

There are no conflicts to declare.

Acknowledgements

References

1 J. R. Rostrup-Nielsen and J. H. B. Hansen, *J. Catal.*, 1993, **144**, 38–49.

2 A. Sternberg and A. Bardow, *ACS Sustainable Chem. Eng.*, 2016, **4**, 4156–4165.

3 V. T. Sagar and A. Pintar, *Appl. Catal., A*, 2020, **599**, 117603.

4 M. A. Álvarez, L. F. Bobadilla, V. Garcilaso, M. A. Centeno and J. A. Odriozola, *J. CO2 Util.*, 2018, **24**, 509–515.

5 Z. Liu, F. Zhang, N. Rui, X. Li, L. Lin, L. E. Betancourt, D. Su, W. Xu, J. Cen, K. Attenkofer, H. Idriss, J. A. Rodriguez and S. D. Senanayake, *ACS Catal.*, 2019, **9**, 3349–3359.

6 M. García-Diéguez, E. Finocchio, M. Á. Larrubia, L. J. Alemany and G. Busca, *J. Catal.*, 2010, **274**, 11–20.

7 B. Bachiller-Baeza, C. Mateos-Pedrero, M. A. Soria, A. Guerrero-Ruiz, U. Rodemerck and I. Rodríguez-Ramos, *Appl. Catal., B*, 2013, **129**, 450–459.

8 M. Németh, Z. Schay, D. Srankó, J. Károlyi, G. Sáfrán, I. Sajó and A. Horváth, *Appl. Catal., A*, 2015, **504**, 608–620.

9 C. C. Chong, Y. W. Cheng, H. D. Setiabudi, N. Ainirazali, D. V. N. Vo and B. Abdullah, *Int. J. Hydrogen Energy*, 2020, **45**, 8507–8525.

10 S. Das, M. Sengupta, A. Bag, M. Shah and A. Bordoloi, *Nanoscale*, 2018, **10**, 6409–6425.

11 H. Chen, S. Chansai, S. Xu, S. Xu, Y. Mu, C. Hardacre and X. Fan, *Catal. Sci. Technol.*, 2021, **11**, 5260–5272.

12 L. F. Bobadilla, J. L. Santos, S. Ivanova, J. A. Odriozola and A. Urakawa, *ACS Catal.*, 2018, **8**, 7455–7467.

13 L. D. Chen, M. Urushihara, K. Chan and J. K. Nørskov, *ACS Catal.*, 2016, **6**, 7133–7139.

14 J. Ran, M. Jaroniec and S. Z. Qiao, *Adv. Mater.*, 2018, **30**, 1704649.

15 W. C. Chung, K. L. Pan, H. M. Lee and M. B. Chang, *Energy Fuels*, 2014, **28**, 7621–7631.

16 X. Gao, Z. Lin, T. Li, L. Huang, J. Zhang, S. Askari, N. Dewangan, A. Jangam and S. Kawi, *Catalysts*, 2021, **11**, 455.

17 X. Zhang, C. S. M. Lee, D. M. P. Mingos and D. O. Hayward, *Catal. Lett.*, 2003, **88**, 129–139.

18 M. Wang, M. Shen, X. Jin, J. Tian, M. Li, Y. Zhou, L. Zhang, Y. Li and J. Shi, *ACS Catal.*, 2019, **9**, 4573–4581.

19 X. Zhu, J. H. Liu, X. S. Li, J. L. Liu, X. Qu and A. M. Zhu, *J. Energy Chem.*, 2017, **26**, 488–493.

20 D. Mei, X. Zhu, Y. L. He, J. D. Yan and X. Tu, *Plasma Sources Sci. Technol.*, 2015, **24**, 015011.

21 X. Tu and J. C. Whitehead, *Appl. Catal., B*, 2012, **125**, 439–448.

22 M. Torimoto, S. Ogo, Y. Hisai, N. Nakano, A. Takahashi, Q. Ma, J. G. Seo, H. Tsuneki, T. Norby and Y. Sekine, *RSC Adv.*, 2020, **10**, 26418–26424.

23 S. Okada, R. Manabe, R. Inagaki, S. Ogo and Y. Sekine, *Catal. Today*, 2018, **307**, 272–276.

24 S. Ogo and Y. Sekine, *Chem. Rec.*, 2017, **17**, 726–738.

25 M. Torimoto, K. Murakami and Y. Sekine, *Bull. Chem. Soc. Jpn.*, 2019, **92**, 1785–1792.

26 T. Yabe, K. Mitarai, K. Oshima, S. Ogo and Y. Sekine, *Fuel Process. Technol.*, 2017, **158**, 96–103.

27 K. Oshima, T. Shinagawa, Y. Nogami, R. Manabe, S. Ogo and Y. Sekine, *Catal. Today*, 2014, **232**, 27–32.

28 K. Yamada, S. Ogo, R. Yamano, T. Higo and Y. Sekine, *Chem. Lett.*, 2020, **49**, 303–306.

29 R. Manabe, S. Okada, R. Inagaki, K. Oshima, S. Ogo and Y. Sekine, *Sci. Rep.*, 2016, **6**, 38007.

30 D. A. Shirley, *Phys. Rev. B: Solid State*, 1972, **5**, 4709–4714.

31 G. Kresse and J. Hafner, *Phys. Rev. B: Condens. Matter Mater. Phys.*, 1993, **47**, 558–561.

32 G. Kresse and J. Hafner, *Phys. Rev. B: Condens. Matter Mater. Phys.*, 1994, **49**, 14251–14269.

33 G. Kresse and J. Furthmüller, *Comput. Mater. Sci.*, 1996, **6**, 15–50.

34 J. P. Perdew, K. Burke and M. Ernzerhof, *Phys. Rev. Lett.*, 1996, **77**, 3865–3868.

35 S. Grimme, J. Antony, S. Ehrlich and H. Krieg, *J. Chem. Phys.*, 2010, **132**, 154104.

36 J. J. Carey and M. Nolan, *Catal. Sci. Technol.*, 2016, **6**, 3544–3558.

37 K. Murakami, Y. Mizutani, H. Sampei, A. Ishikawa and Y. Sekine, *J. Chem. Phys.*, 2021, **154**, 164705.

38 M. D. Krcha, A. D. Mayernick and M. J. Janik, *J. Catal.*, 2012, **293**, 103–115.

39 H. T. Chen and J. G. Chang, *J. Chem. Phys.*, 2010, **132**, 214702.

40 M. Nolan, *J. Mater. Chem.*, 2011, **21**, 9160–9168.

41 A. D. Mayernick and M. J. Janik, *J. Phys. Chem. C*, 2008, **112**, 14955–14964.

42 M. Methfessel and A. T. Paxton, *Phys. Rev. B: Condens. Matter Mater. Phys.*, 1989, **40**, 3616–3621.

43 H. J. Monkhorst and J. D. Pack, *Phys. Rev. B: Solid State*, 1976, **13**, 5188–5192.

44 A. Sundaresan, R. Bhargavi, N. Rangarajan, U. Siddesh and C. N. R. Rao, *Phys. Rev. B: Condens. Matter Mater. Phys.*, 2006, **74**, 161306.

45 I. N. Leontyev, A. B. Kuriganova, N. G. Leontyev, L. Hennet, A. Rakhmatullin, N. V. Smirnova and V. Dmitriev, *RSC Adv.*, 2014, **4**, 35959–35965.

46 K. Momma and F. Izumi, *J. Appl. Crystallogr.*, 2011, **44**, 1272–1276.

47 K. Takise, A. Sato, K. Murakami, S. Ogo, J. G. Seo, K. I. Imagawa, S. Kado and Y. Sekine, *RSC Adv.*, 2019, **9**, 5918–5924.

48 M. Daturi, C. Binet, J. C. Lavalley and G. Blanchard, *Surf. Interface Anal.*, 2000, **30**, 273–277.

49 L. Fan, J. Zhang, K. Ma, Y. Zhang, Y. M. Hu, L. Kong, A. ping Jia, Z. Zhang, W. Huang and J. Q. Lu, *J. Catal.*, 2021, **397**, 116–127.

50 L. Atzori, M. G. Cutrufello, D. Meloni, B. Onida, D. Gazzoli, A. Ardu, R. Monaci, M. F. Sini and E. Rombi, *Front. Chem. Sci. Eng.*, 2021, **15**, 251–268.

51 Z. Wu, A. K. P. Mann, M. Li and S. H. Overbury, *J. Phys. Chem. C*, 2015, **119**, 7340–7350.

52 Z. Wu, M. Li and S. H. Overbury, *J. Catal.*, 2012, **285**, 61–73.

53 T. Shido and Y. Iwasawa, *J. Catal.*, 1993, **141**, 71–81.

54 S. Y. Zhao, S. P. Wang, Y. J. Zhao and X. Bin Ma, *Chin. Chem. Lett.*, 2017, **28**, 65–69.

55 Z. Wu, M. Li and S. H. Overbury, *J. Catal.*, 2012, **285**, 61–73.

56 K. Yoshikawa, H. Sato, M. Kaneeda and J. N. Kondo, *J. CO2 Util.*, 2014, **8**, 34–38.

57 Y. Wang, Z. Liu, M. P. Confer, J. Li and R. Wang, *Mol. Catal.*, 2021, **509**, 111629.

58 O. Pozdnyakova, D. Teschner, A. Wootsch, J. Kröhnert, B. Steinhauer, H. Sauer, L. Toth, F. C. Jentoft, A. Knop-Gericke, Z. Paál and R. Schlögl, *J. Catal.*, 2006, **237**, 1–16.

59 P. A. U. Aldana, F. Ocampo, K. Kobl, B. Louis, F. Thibault-Starzyk, M. Daturi, P. Bazin, S. Thomas and A. C. Roger, *Catal. Today*, 2013, **215**, 201–207.

60 P. Bea, A. L. Camera, A. Hornes and A. Martınez-Arias, *J. Phys. Chem. C*, 2009, **113**, 10689–10695.

61 S. M. Lee, Y. H. Lee, D. H. Moon, J. Y. Ahn, D. D. Nguyen, S. W. Chang and S. S. Kim, *Ind. Eng. Chem. Res.*, 2019, **58**, 8656–8662.

62 F. C. Meunier, D. Tibiletti, A. Goguet, D. Reid and R. Burch, *Appl. Catal., A*, 2005, **289**, 104–112.

63 G. Busca and V. Lorenzelli, *Mater. Chem.*, 1982, **7**, 89–126.

64 S. Hilaire, X. Wang, T. Luo, R. J. Gorte and J. Wagner, *Appl. Catal., A*, 2004, **258**, 271–276.

65 T. Tabakova, F. Boccuzzi, M. Manzoli and D. Andreeva, *Appl. Catal., A*, 2003, **252**, 385–397.

66 C. Li, Y. Sakata, T. Arai, K. Domen, K. I. Maruya and T. Onishi, *J. Chem. Soc., Faraday Trans. 1*, 1989, **85**, 1451–1461.

67 L. Chen, S. Wang, J. Zhou, Y. Shen, Y. Zhao and X. Ma, *RSC Adv.*, 2014, **4**, 30968–30975.

68 M. Wang, M. Shen, X. Jin, J. Tian, Y. Shao, L. Zhang, Y. Li and J. Shi, *Chem. Eng. J.*, 2022, **427**, 130987.

69 Q. Pan, J. Peng, S. Wang and S. Wang, *Catal. Sci. Technol.*, 2014, **4**, 502–509.

70 G. Finos, S. Collins, G. Blanco, E. Del Rio, J. M. Cíes, S. Bernal and A. Bonivardi, *Catal. Today*, 2012, **180**, 9–18.

71 C. Li, Y. Sakata, T. Arai, K. Domen, K. I. Maruya and T. Onishi, *J. Chem. Soc., Faraday Trans. 1*, 1989, **85**, 929–943.

72 A. Yee, S. J. Morrison and H. Idriss, *J. Catal.*, 1999, **186**, 279–295.

73 C. Binet, M. Daturi and J. C. Lavalley, *Catal. Today*, 1999, **50**, 207–225.

74 G. Ramis, G. Busca and V. Lorenzelli, *Mater. Chem. Phys.*, 1991, **29**, 425–435.

75 T. Yabe, K. Yamada, K. Murakami, K. Toko, K. Ito, T. Higo, S. Ogo and Y. Sekine, *ACS Sustainable Chem. Eng.*, 2019, **7**, 5690–5697.

76 B. Liu, C. Li, G. Zhang, X. Yao, S. S. C. Chuang and Z. Li, *ACS Catal.*, 2018, **8**, 10446–10456.

77 Z. Ma, P. Li, L. Ye, Y. Zhou, F. Su, C. Ding, H. Xie, Y. Bai and P. K. Wong, *J. Mater. Chem. A*, 2017, **5**, 24995–25004.

78 K. Kousi, D. Neagu, L. Bekris, E. I. Papaioannou and I. S. Metcalfe, *Angew. Chem.*, 2020, **132**, 2531–2540.

79 K. Sutthiumporn, T. Maneerung, Y. Kathiraser and S. Kawi, *Int. J. Hydrogen Energy*, 2012, **37**, 11195–11207.

80 L. Óvári, S. Krick Calderon, Y. Lykhach, J. Libuda, A. Erdohelyi, C. Papp, J. Kiss and H. P. Steinrück, *J. Catal.*, 2013, **307**, 132–139.

81 Y. Yu, B. Mao, A. Geller, R. Chang, K. Gaskell, Z. Liu and B. W. Eichhorn, *Phys. Chem. Chem. Phys.*, 2014, **16**, 11633–11639.

82 F. Chen, D. Liu, J. Zhang, P. Hu, X. Q. Gong and G. Lu, *Phys. Chem. Chem. Phys.*, 2012, **14**, 16573–16580.

83 A. Sato, S. Ogo, Y. Takeno, K. Takise, J. G. Seo and Y. Sekine, *ACS Omega*, 2019, **4**, 10438–10443.

84 Y. Omori, A. Shigemoto, K. Sugihara, T. Higo, T. Uenishi and Y. Sekine, *Catal. Sci. Technol.*, 2021, **11**, 4008–4011.

85 K. Sugiura, S. Ogo, K. Iwasaki, T. Yabe and Y. Sekine, *Sci. Rep.*, 2016, **6**, 25154.

86 S. Das, A. Jangam, S. Jayaprakash, S. Xi, K. Hidajat, K. Tomishige and S. Kawi, *Appl. Catal., B*, 2021, **290**, 119998.

87 J. H. Bitter, K. Seshan and J. A. Lercher, *Top. Catal.*, 2000, **10**, 295–305.

88 K. Otsuka, Y. Wang, E. Sunada and I. Yamanaka, *J. Catal.*, 1998, **175**, 152–160.

89 J. Wei and E. Iglesia, *J. Phys. Chem. B*, 2004, **108**, 4094–4103.

90 A. P. Ferreira, I. Rodriguez-Ramos, J. A. Anderson and A. Guerrero-Ruiz, *Appl. Catal., A*, 2000, **202**, 183–196.